Highlights

From Soil to Printed Structures: A Systematic Approach to Designing Clay-Based Materials for 3D Printing in Construction and Architecture

Ofer Asaf, Arnon Bentur, Pavel Larianovsky, Aaron Sprecher

- Flow-table and rigidity test evaluate mixture performance at green state.
- Clay particle grading and composition impact rheological properties and printing performance.
- Analytical model predicts stability and failure of 3D printed soil elements.
- Identified disparity between green and hardened states of clay mixes in 3D printing.

From Soil to Printed Structures: A Systematic Approach to Designing Clay-Based Materials for 3D Printing in Construction and Architecture

Ofer Asaf[a], Arnon Bentur[b], Pavel Larianovsky[b], Aaron Sprecher[a]

[a] *Faculty of Architecture and Town Planning, Technion - Israel Institute of Technology, Haifa, 3200003, Israel*
[b] *Faculty of Civil and Environmental Engineering, Technion - Israel Institute of Technology, Haifa, 3200003, Israel*

Abstract

3D printing of clayey soils has gained traction in construction and architecture due to its eco-friendly and design advantages. However, comprehensive method for transforming these soils into a mix that exhibits flow and stability is limited. To this end, a series of tests were conducted on 12 mixes of sand and clay. These mixes were tested for their rheological properties and performance in rigidity and pumping tests. Linear relationships between the various results were compared. This was followed by an in-situ printing test. An analytical model for predicting the plastic collapse of the bottom layer was employed. To better elucidate the failure mechanism, digital image correlation was used. Finally, the mechanical properties of the mixes were assessed at 14 and 28 days. The results indicate that using values obtained from flow-table test and custom rigidity test, effectively optimizes a mix for 3D printing. Rheological findings show that increased kaolinite enhances the thixotropic effect of the mix. Coarser particle size distribution improves static yield due to elevated interparticle friction. In-situ printing tests suggest that a rotational rheometer test can predict element failure from plastic collapse according to the printing parameters. Finally, mechanical properties reveal a disparity between fresh and hardened properties of the clay-soil mixes.

Keywords: 3D printing, Soil-based materials, Buildability, Robotic fabrication, Earth construction

1. Introduction

Additive manufacturing, often referred to as 3D printing, using clayey soils, has gained increased interest in the architectural and construction sector [1, 2, 3, 4]. Several prominent factors drive this growing interest. Firstly, 3D printing technologies, lauded for their advanced design capabilities, empower architects and engineers to actualize optimized, innovative structures [5, 6]. Secondly, escalating environmental concerns related to the building sector have catalyzed a search for sustainable materials [7]. In this context, soils emerge as an alternative to traditional construction materials, owing to their reduced environmental footprint [8, 9], and their adaptability within a circular economy framework [10, 11].

The synergy between 3D printing and using soils as construction materials presents extensive application opportunities, ranging from small-scale elements to large-scale structures. Examples of these structures include integrated wall components [12], elements designed for green infrastructure [13], structures aimed at providing low-impact affordable housing [14], and architectural edifices [15]. Moreover, 3D printing of soils also captures interest for extraterrestrial construction [16, 17]. In these scenarios, local regolith, rich in amorphous inorganic compounds, promises potential transformation by alkalis into geopolymer binders [18]. All these applications underscore the need for clear guidelines to convert local soils into 3D printable mixtures [19].

For designing such materials, understanding their rheological properties is essential [20, 21]. These properties govern the material's transportation through the pumping system and determine the stability of the layer post-deposition [22]. A 3D printable material should demonstrate two contrasting characteristics that necessitate a balance: the ability to flow through the pumping system and rigidity upon deposition. In order to initiate flow of the material, a critical shear stress is delineated as the static yield stress (τ_{0s}). must be surpassed before the material starts to flow. Following that stage, the mixture enters a dynamic state where a linear relationship is exhibited between the shear strain and shear stress. This association is described according to Bingham model[23]. The magnitude of this relation can be expressed by the material's apparent viscosity μ. The intersection of this linear relation is expressed as the dynamic yield stress (τ_{0d}) of the material [24].

In terms of material processing, when the material is conveyed to the printhead, a phenomenon known as ”plug flow” is observed due to the material's heightened viscosity [25]. This flow state results in pressure loss, primarily due to particle friction against the delivery hose. Such friction subsequently slows down the flow rate and necessitates more energy from the pump. For materials that align with the Bingham model, their pressure loss when flowing inside a conduit is determined by two factors: yield stress and viscosity. This relationship can be described using the Buckingham-Reiner model [26]. Ideally, to ensure a smooth and efficient flow, a mixture should have both a low dynamic yield stress and low viscosity. Yet, after being extruded from the nozzle, it is crucial for the material to quickly elevate its static yield stress to retain stability. The difference in behavior between these static and dynamic properties is referred to as the material's thixotropy. Consequently, an optimal 3D printing material should demonstrate a rapid increase in thixotropic behavior without a corresponding rise in its dynamic properties. While cement-based systems often exhibit this thixotropic nature [27, 28], such behavior is less commonly seen in clay-based mixtures during printing [29].

For cementitious systems, the rheological properties required for the 3D printing process have been considerably discussed. Roussel introduced a theoretical model for printable concrete that is rooted in rheology[30]. This model aims to prevent critical strain, which could result in the collapse of the printed bottom layer. Kruger et al. put forth an analytical model to ascertain layer stability during the printing process, grounded in rheological testing [31, 32]. Their model leverages static yield stress and a correction factor tied to the layer's cross-section. It can predict, with a commendable level of accuracy, the potential failure of a printed artifact when its self-weight surpasses the static yield. Furthermore, Kruger applied this model to pinpoint optimal printing parameters [33]. In the context of earth-based materials, Perrot et al. employed a similar methodology to evaluate the buildability of a soil-based mixture, though they did not conduct in-situ 3D printing tests [29].

In the realm of 3D printing of soils, literature sought to design optimal soil-based mixtures. Several methods have been proposed to imbue these mixtures with the rheological properties essential for 3D printing. Perrot et al. highlighted the use of alginate bio-polymer to induce a thixotropic effect in earth-based mixtures and analyzed the mix based on a penetrometer test [29]. Biggerstaff et al. employed a rotational rheometer to estimate the yield stress of bio-polymer bound soil mixtures [34, 35]. Bajpayee et al. charted a holistic approach for 3D printing soil, comprising particle distribution analysis, mineralogical composition analysis and rotational rheometer for using geopolymerization reaction [36]. Silva et al. turned to a shear-vane test and a custom stability test to evaluate the fresh state properties of the mix [37]. Alqenaee et al., using a deformation test introduced by [38], explored the various aspects of mixture design [39]. In a different vein, Ferreti et al. utilized rice husk and hydraulic lime to enhance the material's hardened properties [40]. Faleschini showcased the incorporation of lime, cement, and vegetable fiber to optimize both the mechanical and economic properties of the mix [41]. Nevertheless, a comprehensive method that unifies basic tests with in-situ printing evaluations tailored for designing 3D printable clayey soils remains absent. The short-term rheological characteristics of clay-based materials, crucial for predicting construction speeds [30], are yet to be thoroughly examined. Furthermore, despite their heterogeneous nature, the impact of mineralogical and physical variations in local soils on 3D printing largely remains understudied [42, 43, 44].

Consequently, there is a need for fundamental guidelines for designing and evaluating soil-based mixtures for 3D printing reflecting their shared characteristics. These guidelines could be a foundational reference for designing and developing such materials. The primary contribution of this study is to identify a shared framework for developing soil-based mixtures and setting the right printing parameters for 3D printing applications in construction. In doing so, this research strives to lay the groundwork for refining 3D printing of soils, considering both material progression and the printing parameters. Multiple mixtures were developed with different particle grading and water content. These were assessed using simple testing methods, rotational rheological tests, and performance values. Linear correlations emerged between the different testing methods and performance values, providing guidelines to find the best performance window for any specified printing equipment. Three different clay types were then tested to gauge the influence of mineralogical and particle grading on the printing behavior. In-situ cylinder printing was utilized to predict the collapse of the layers buildup based on rheological properties. Lastly, the study delves into the effect of clay type on the mechanical properties of the different clays, suggesting a tension between optimizing the green and hardened properties of the mixture.

2. Materials and methods

Figure 1 describes the step-by-step experimental method followed in this study.

2.1. *Materials*

The tested mixtures comprised of quartz dune sand and three distinct types of powdered clays. Quartz dune sand (Sand) was sourced from Kfar Giladi Minerals and sieved through a 1.18 mm sieve. White kaolinite clay (White) was procured from Alco Chemicals. Brown-red kaolinite clay (Chocolate) and yellow marl clay (Mamshit) were obtained from Yehu Clays Ltd.

2.2. *XRD analysis*

A McCrone micronizing device with 16 agate was used to wet-grind the clays. During each preparation, 6 g of each sample and 15 ml of isopropanol were added as griding media. The samples were ground at 1500 rpm for 15 minutes. After the milling, the clays were filtered in a Whatman grade 3 filter paper (6 µm pore size) using a vacuum pump, rinsed with diethyl ether, and dried for 15 min at 40 °C in a vacuum oven at a constant pressure of 300 mbar. X-ray powder diffraction (XRPD) using a PANalytical EMPYREAN X-ray diffractometer equipped with a Cu-Kα1,2 radiation tube (λ = 1.5408 Å). The XRD optical configuration for the incident beam consisted of a 10 mm mask, 0.04 rad Soller slit along with 1/16° divergence and 1/8° anti-scatter fixed slits. The diffracted beam optics comprised a 7.5 mm anti-scatter fixed slit and 0.04 rad Soller slit. The XRD data were collected at 45 kV accelerating voltage and 40 mA current in a conventional Bragg-Brentano θ-2θ geometry. The samples were scanned with a PIXcel 3D detector for data acquisition. All scans were measured using a continuous scan mode over an angular range of 5° to 70° (2θ) with 0.017°2θ step size for approximately 20 min per scan for Kaoline (18-2023) the range was of with 3-75 (2θ) with the same step, 0.017°2θ. Quantitative phase analysis was performed by the Rietveld refinement method as implemented in the HighScore

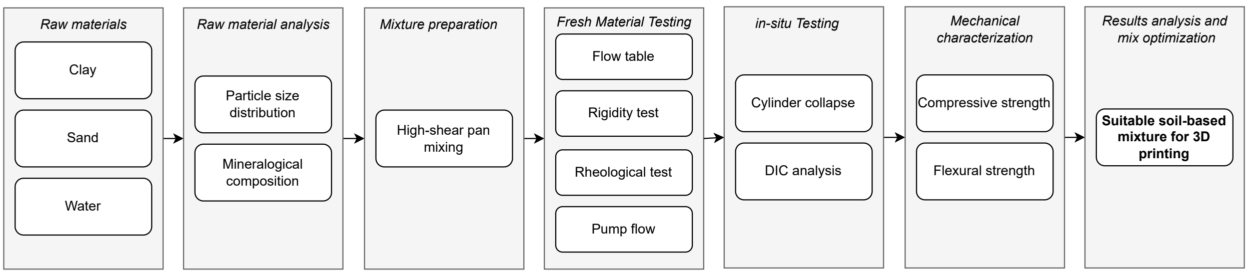

Figure 1: Flow chart illustrating the step-by-step experimental method used in the study.

Plus software (Malvern Panalytical).

Table 1: Mineralogical composition of raw powdered clay mixtures.

Phase	Kaolinite	Quartz	Calcite	Illite	Muscovite	Ivsite	Picromerite	Orthoclase
Sand	0	99.9	0.1	0	0	0	0	0
White	99.4	0.4	0	0	0.2	0	0	0
Chocolate	76.8	12.7	1.4	0	0	3.9	3.1	2.1
Mamshit	41.5	17.0	22.9	7.0	5.0	0	0	6.2

2.3. Particle size distribution

A Laser diffractometer Mastersizer 3000 Particle Size Analyzer (Malvern Panalytical) was used to analyze the particle size distribution. 0.1 grams of sample were mixed with 10 ml of isopropanol, followed by 30 seconds of sonication to avoid aggregate formation. The mixture was slowly added to the Hydro LV device.

2.4. Mixture preparation

The mixtures were prepared with a high-shear pan mixer. The mixer tank was first filled with all dry ingredients, after which the water was added. The clay/sand and clay/water ratios of the mixture are described in Table 2. Following the addition of water the materials were intensively mixed for 3 minutes. The mixer was inspected to ensure that no dry ingredients were left unmixed before continuing with another 6 minutes of high-shear mixing.

2.5. Test methods of green material

The test methods of the fresh green material included ones that can provide basic physical and mechanical parameters of the material for 3D printing, as well as standard tests which can be used for comparison and characterization of properties.

Flow test was conducted using the ASTM C230 flow table test for hydraulic cement [45], as shown in Figure 3a. A brass conical mold was placed at the center of the table and filled with the mixture. The mold was then removed and the table was jolted 25 times and the spread of the material was recorded.

Table 2: Composition of tested white clay-sand mixtures.

Mix	Clay (wt.%)	Sand (wt.%)	Water (wt.%)
M1	19.41	65.50	15.09
M2	21.62	62.45	15.93
M3	24.03	60.07	15.91
M4	23.44	58.60	17.96
M5	23.89	59.72	16.39
M6	24.18	60.44	15.38
M7	24.03	60.07	15.91
M8	28.26	54.17	17.57
M9	28.60	54.61	16.79
M10	30.37	51.40	18.22
M11	32.97	49.46	17.57
M12	32.74	49.11	18.15

The rigidity of the fresh green mix was characterized using the loading apparatus shown in Figure 3b, following Kazemian et al. [46]. During the test, a cylindrical mold with a diameter of 185 mm and a height of 100 mm was used. The mold was first filled with fresh material in two stages to ensure proper packing, followed by removal of the mold. A transparent board was placed on top of the material, which was loaded with an incremental increase of 500 gr weights equivalent to 0.18 kPa. The deformation at four corners of the board was measured and the average deformation was recorded. The test continued up to a load of 2.9 kPa. Load-deformation curves were obtained, and the rigidity coefficient, defined as the slope of the curve, was calculated.

Rheological test was carried out using a commercialized rotational rheometer, ICAR Plus (Germann Instruments Inc.), as shown in Figure 3c. The geometry of the rheometer consists of a 4-bladed vane located at the center of a cylindrical container. The test was performed in two modes, stress growth test to determine the static yield strength, and flow curve test to determine the dynamic yield strength and apparent viscosity.

In the stress growth test, the vane rotation was set to a constant value of 0.16 rad/s, and the static yield stress is computed according to Eq. 1.

$$\tau_{0s} = \frac{2T}{\pi D^3 \left(\frac{H}{D} + \frac{1}{3}\right)} \tag{1}$$

Where τ_{0s} is the static yield stress, T is the maximum torque value recorded, D is the vane's diameter and H is the vane's height.

In the flow curve test, varying rotation rates, 0.31 to 3.14 rad/s, subject the mixture to different shear strain rates. This led to a stress shear-strain rate, or rotation rate curve, that exhibited a linear pattern which could be described by the Bingham model as described in Equation 2. For all mixtures analyzed, a R^2 value of no less than 0.95 was observed, pointing to a pronounced linear association between shear stresses and shear strain rates. As such, the flow curve test characterized the two dynamic rheological parameters: dynamic yield stress and apparent coefficient of viscosity.

$$\tau = \tau_{0d} + \mu\dot{\gamma} \tag{2}$$

Where τ_{0d} is the dynamic yield stress, μ is the Plastic viscosity and $\dot{\gamma}$ is the shear strain rate.

The abovementioned rheological measurements were conducted at specific time intervals (0, 0.5, 1, 2, 5, 10, 15, 30, 45 min), with the material remaining stationary in the rheometer during the intervals. This resting period allowed for the development of physical bonds between particles and simulated the time elapsed following material deposition from the nozzle in a 3D printing process.

To evaluate the ability to transport the material through the delivery system, the flow rate of the pump (Figure 4) was recorded at a set voltage value (5V) supplied to the pump control unit.

2.6. Statistical Analysis for Linear Correlation

A statistical analysis was conducted using the NumPy and Matplotlib libraries for Python to evaluate linear correlations between the composition, rheological characteristics, and performance parameters of the mixtures. The strength and direction of these linear relationships were quantified by calculating Pearson's r correlation coefficient, as described in Equation 3. This coefficient ranges between -1 and 1, indicating the extent of linear association between two datasets [47]. The aim of the analysis was to identify potential patterns and dependencies, shedding light on how the mix's composition and rheological characteristics influence its performance parameters.

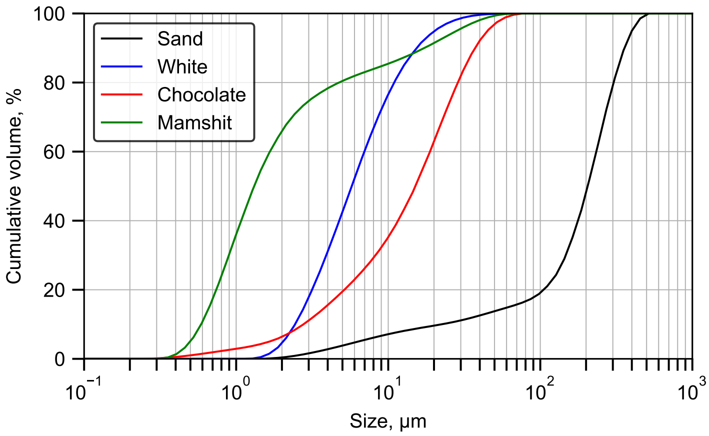

Figure 2: Particle size distribution of raw materials.

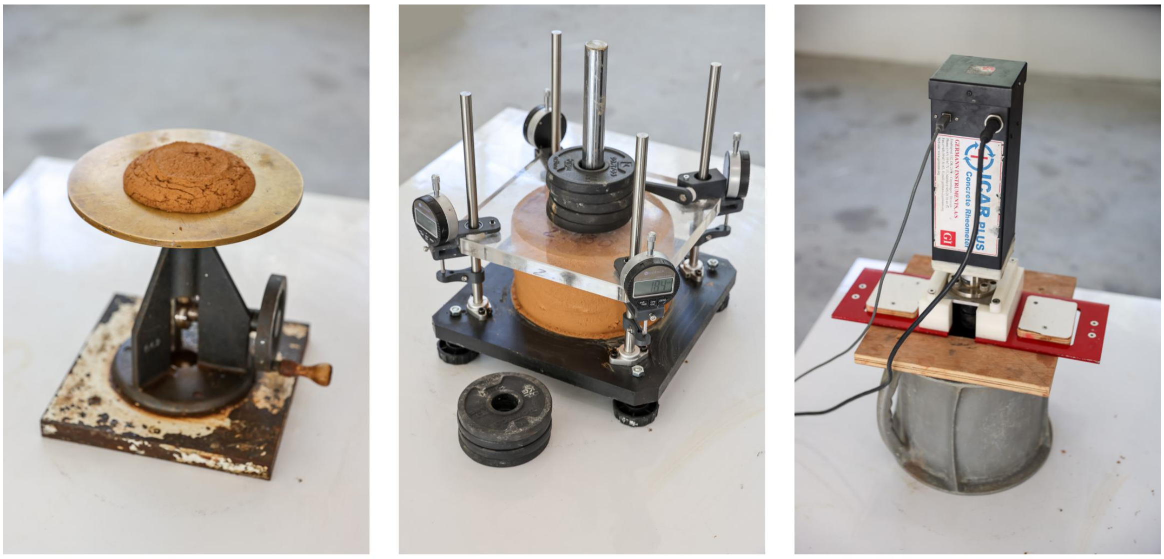

a) b) c)

Figure 3: Green material test methods: a) Flow table test, assessing flow properties through the mix spread after jolting; b) Fresh green material loading rig, measuring rigidity via deformation under incremental load increases; c) ICAR rheometer, evaluating static and dynamic rheological properties of the mix.

$$r = \frac{\sum(x_i - \bar{x})(y_i - \bar{y})}{\sqrt{\sum(x_i - \bar{x})^2 \sum(y_i - \bar{y})^2}} \tag{3}$$

Where x_i and y_i are individual data points and $\bar{x}$ is the mean of the x-values and $\bar{y}$ is the mean of the y-values.

2.7. In-situ testing

In-situ testing involved printing cylindrical samples with a diameter of 180 mm. To continuously monitor the layer heights during the printing process, 30 frame per second video recording was employed. A Canon 6D camera, equipped with a Canon EF 70-200/2.8L IS II lens, was positioned to capture detailed footage of each layer as it was printed. This allowed us to closely inspect of the print layers throughout the procedure. The experiment continued until the cylinder collapsed, at which point the time to failure and the number of layers at failure was recorded. A digital analysis of the printing process was conducted with digital image correlation software, Tema PRO by ImageSystems, to evaluate the deformation of the lower layers during printing.

2.8. Mechanical characterization

For mechanical characterization, specimens from each mixture were prepared in accordance with standards EN 12350-1 for compressive strength and EN 12390-5 for flexural strength. The dimensions of the test specimens were 50 x 50 x 50 mm for the compressive strength test and 40 x 40 x 160 mm for the flexural strength test. It should be noted that these dimensions, while effective for our experimental objectives, do not strictly conform to standard sizes for earthen materials. After 24 hours post-casting, the samples were demolded and subsequently subjected to drying for 14 days in a controlled laboratory environment, maintaining a temperature of 21 °C and a relative humidity of 50

A 500 kN MULTIPURPOSE 500 (CONTROLS Group) compression-flexure cement testing frame was used to evaluate the compressive and flexural strength of the specimens. Two steel plates, each measuring 40 x 40 mm with a height of 10 mm, were employed during testing. Each specimen was centrally positioned on these plates, and the load was progressively increased at a

Figure 4: Robotic cell setup for 3D printing of clayey soils, featuring an industrial robotic arm, mortar pump, and concrete vibrator.

rate of 0.5 MPa per second. The uniaxial compressive strength of the specimens was determined by the peak force recorded by the machine at the moment of specimen failure.

2.9. 3D printing setup

The robotic setup used for this research is shown in Figure 3. The setup includes a KUKA KR50R2100 industrial robotic arm, featuring a payload of 50 kg and a radial range of 2100 mm. The printhead used for printing comprised a 450mm long metal rod, which was mounted perpendicularly to the robot flange. The nozzle used in the printhead was 3D printed from PET-G and featured a diameter of 12.5 mm. The mortar pump used for the printing process was MAI 2PUMP-PICTOR, with a 24L worm pump, featuring a flow rate of 1.5-8.5 L/min. A concrete vibrator was used to promote the mixture flow from the hopper to the worm pump. A GW Instek DC power supply was connected to the pump to control the flow rate by altering the supplied voltage. A 10-meter high-pressure hose was used for delivering the mixture from the pump to the printhead mounted on top of the robotic arm.

3. Results and discussion

3.1. Rheological properties and mix performance at green-state

3.1.1. Rheological behavior

Typical results of the rheological parameters as a function of resting time are shown in Figure 5. The time scale represents the resting time between consecutive measurements, up to 45 minutes. The cumulative time since the end of mixing was longer, totaling 110 minutes.

In the studied clay-based systems, the static shear yield stress can be analyzed in terms of its development over two stages: re-flocculation and structuration. During the re-flocculation stage, which occurs within the first few minutes, the increase in static shear yield stress is attributed to microstructural recovery of the platy clay particles, flocculation of the soil's particles and a change in the adsorbed water structure [48, 49]. Following re-flocculation, the structuration stage involves further increases in static shear yield stress, due to material dehydration and compaction over time. The structuration of non-stabilized clay system is not significant within the test period in this study [29].

The dynamic state of the mixture occurs as sufficient shear stress is applied to the mixture and the bonds between the particles break. The dynamic yield value and apparent viscosity characterize the mixture at this stage. In the studied systems, the dynamic parameters stay stable throughout the test, as seen in Figure 5. The difference between static and dynamic shear yield stresses reflects the thixotropic nature of the system, which is crucial for the manufacturing process.

3.1.2. Relations between the rheological parameters and performance values

The rheological characteristics of the mixtures were compared with actual performance parameters. For that purpose, a series of tests were carried out with 12 clay mix compositions, changing the ratio between the white-kaolinite clay and sand, as well as the content of water over a wide range (Table 2). The effect of the mix composition was characterized by a variety of tests: rheological tests, which provide fundamental physical parameters, performance tests which include flow table test, flow rate measurement through the printing nozzle, and the rigidity of the material using the test presented in Figure 3. The correlations between the composition, rheological characteristics and performance parameters are described in Figure 6.

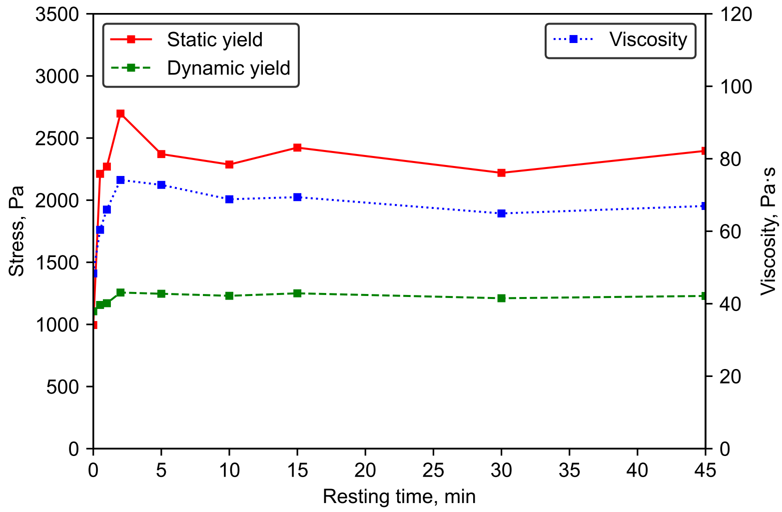

Figure 5: Evolution of rheological parameters in clayey soils over resting time, showcasing the results for white kaolinite clay and sand mixtures.

Significant linear relations were found between the flow rate and apparent viscosity (-0.9), and the flow rate and static yield (-0.87) as shown in Figure 7. The strong negative relation between the viscosity, static yield and the flow rate is typical for materials following the Bingham model [25, 22]. This relationship emphasizes the critical role that viscosity plays in determining the effectiveness of material delivery during 3D printing.

The rigidity of the fresh mix was determined by loading the green material with increasing load as described in Figure 3. The loading test was done manually, with the test lasting about 10 minutes. Under such regime of loading of a viscoelastic material, the rigidity coefficient can be considered as an apparent modulus of the mixture, since the deformations registered include both elastic and plastic deformations. The values measured in this test ranged between 10-120 kPa, which is agreeable with findings reported in literature for 3D printing of clayey soils [29]. The strongest relation was found between the rigidity coefficient and the static yield value (0.97), as shown in Figure 7. This relation can be attributed to the nature of the test, which was incremental and load dependent, therefore influenced highly by the static yield of the material. A controlled deformation test can also be employed for a more precise analysis of the viscoelastic properties of such mixture [50, 51].

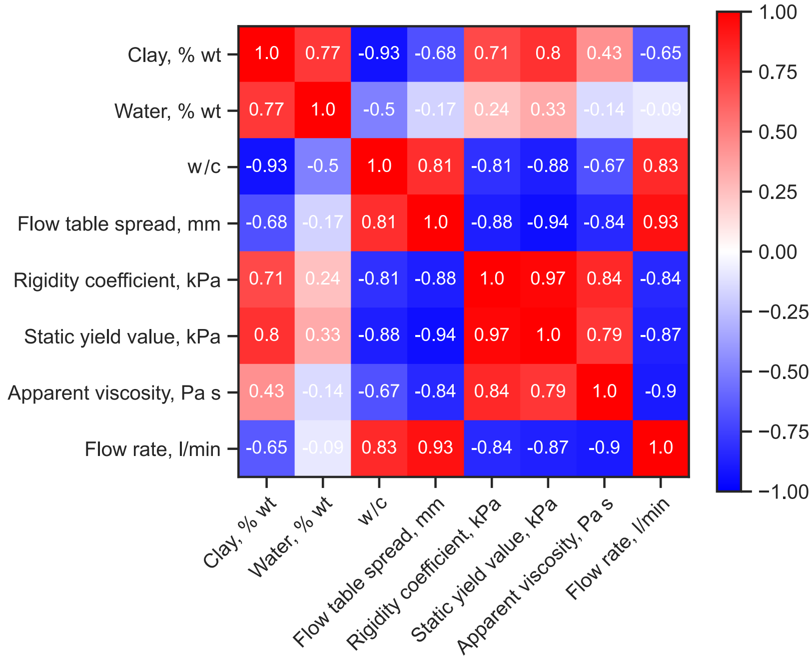

Figure 6: Statistical analysis results for performance parameters in clay mix systems with varying composition, encompassing a range of water/clay and sand/clay ratios as well as clay content in the mix.

3.1.3. Relations between performance values and testing methods

The use of clayey soils in 3D printing mixtures often calls for quick, cost-effective on-site assessments. The statistical analysis, depicted in Figure 8, reveals a strong linear correlation between the spread value from the flow table test, material rigidity coefficient (-0.88), and the flow rate in the pump (0.93). This evidence suggests that a flow table test could be a reliable and practical method for assessing both material flow rate through the nozzle and material rigidity on sit.

As previously discussed, the flow rate, driven by dynamic rheological parameters, is a crucial factor in 3D printing processes. On the other hand, material rigidity is essential to ensure the printed layers retain their intended shape. Therefore, the ability to quickly and efficiently evaluate these characteristics on-site can significantly improve the efficacy and quality of the 3D printing process.

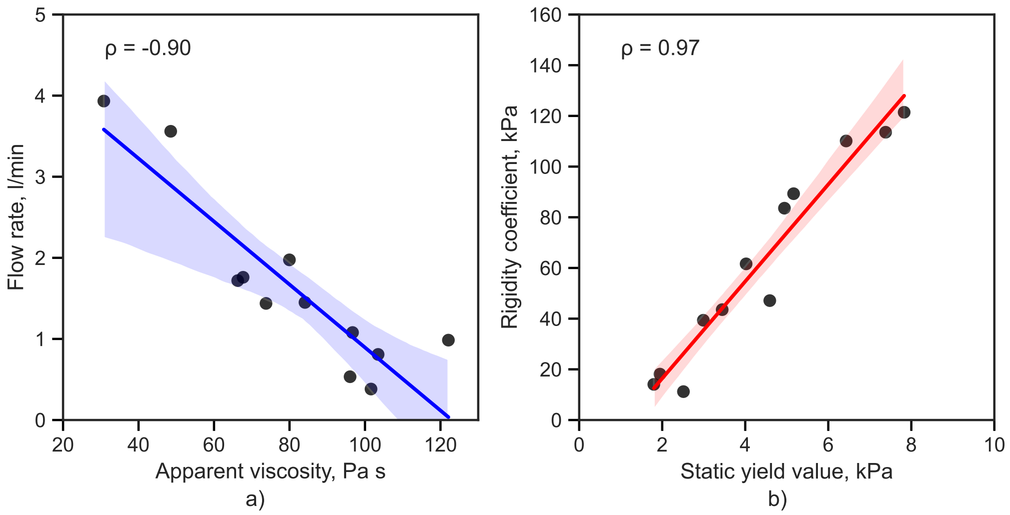

Figure 7: Relations between basic rheological and engineering parameters which are statistically significant: (a) Relation between flow rate through the printing nozzle head and the apparent coefficient of viscosity for clay systems, and (b) Relation between the rigidity of the green material and the static shear yield strength. The highlighted area represents a 95% confidence interval for that relation.

3.1.4. Relations between performance values and of mix composition

The impact of mix composition on material performance is described in Figure 9. The findings reveal a moderate positive correlation between the clay/water ratio and the pump flow rate (0.83). As expected, increasing water content reduces friction between particles, which improves flow. The relationship between the clay weight percentage and the flow rate was less pronounced (-0.65), suggesting that water content is the more influential factor in this process.

Unlike traditional earth construction methods, where optimal moisture content is typically determined based on maximum dry density [43, 52, 53], the moisture content in 3D printing should be evaluated with respect to process performance, to balance the flow properties and material rigidity. Furthermore, the rigidity of the mixture showed a moderate negative correlation with the clay/water ratio (-0.81). In this instance, increasing water content decreases particle friction, thus reducing material rigidity. Conversely, a mild positive relationship was observed between the clay weight percentage and rigidity (0.71).

These results underscore the intricate dynamics between the mix components. Therefore, the optimal balance for 3D printing mixtures will likely depend on carefully tuning these ratios to

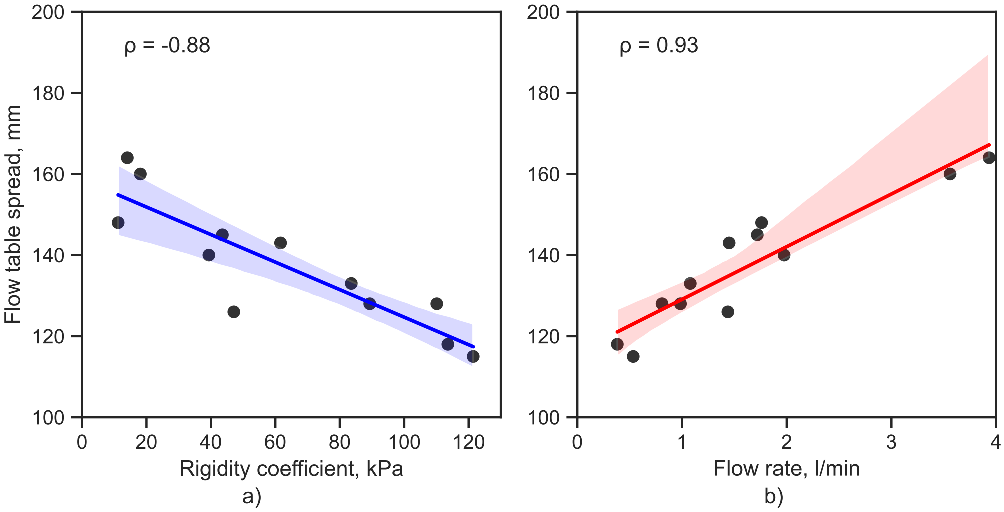

Figure 8: Relations between performance values and testing methods which are statistically significant: (a) Relation between the rigidity coefficient and the spread in flow table test, and (b) Relation between the flow rate through the nozzle and the and the spread in flow table test. The highlighted area represents a 95% confidence interval for that relation.

accommodate both process requirements and desired material properties.

3.2. Design principles

3.2.1. Design principles of the clayey soil mix

The statistical analysis of relationships between rheological and performance parameters, as presented in Section 3.1, can serve as a foundation for insights that can be utilized for optimal mix design of clayey soils for 3D printing applications. The analysis above implies that the overall performance of the mix can be assessed by simultaneously considering two performance tests: the flow table test, which provides an indication of flow through the pumping system, and the rigidity test, which offers insight into the stability of printed layers in the green state.

The relationships between these two parameters for the clay systems studied here are illustrated in Figure 10, highlighting the systems that demonstrated adequate performance for 3D printing. The figure also indicates an optimal performance window, that is, values of a mix that provides a suitable combination of flow and rigidity to facilitate optimal early-age behavior, enabling both pumping and stability in the buildup of printed layers. The various tested mixes were characterized

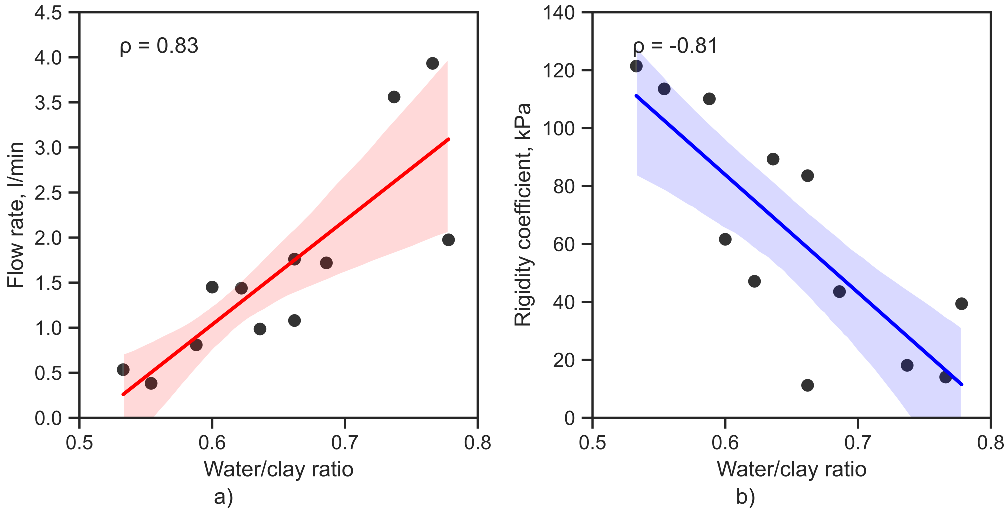

Figure 9: Relations between performance values and mix composition which are statistically significant: (a) Relation between the flow rate through the nozzle and the water/clay ratio, and (b) Relation between the apparent modulus and the water/clay ratio. The highlighted area represents a 95% confidence interval for that relation.

based on their visual appearance, performance in the green method tests, and their ability to be pumped through the delivery system and characterized as either ‘good’, ‘dry’, or ‘unstable’. This approach of identifying a performance window based on relatively simple laboratory performance tests can be highly practical as a guideline for developing optimal mixes. However, it is important to note that such a window serves as a ”fingerprint” specific to a particular printing technology. Factors like different printing systems (e.g., pumping system, printing head, and nozzle) and element size and quality can affect the described window. Consequently, for different printing technologies and elements, a specific ”window” needs to be developed

3.2.2. Effect of particle grading

The mix with a clay content of 28.6%, which resides within the defined ”optimal window” in Figure 10, appears to demonstrate optimal grading. This blend, possessing a water/clay ratio of 0.66, produced the most favorable outcomes regarding pump flow, while simultaneously ensuring satisfactory stability. The particle grading of this mixture is presented in Figure 11. This observation underscores the role that grading plays in influencing a mix’s performance within 3D printing applications. Clay particles enhance the flow within the pumping system by forming a

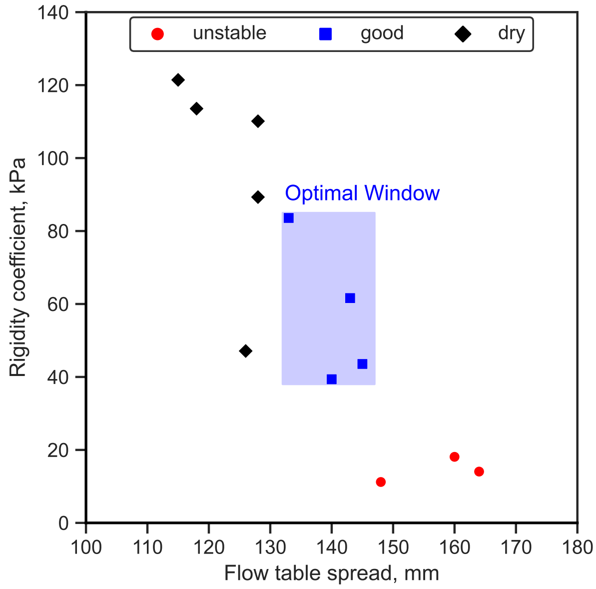

Figure 10: Plot of performance parameters, rigidity and flow, representing different compositions of the clay mix system (white clay/kaolinite-sand-water) and identifying a "window" of adequate overall performance for 3D printing.

lubricating layer. This layer formation results from the clay-water paste migration in response to inhomogeneous shear stresses present in the pipe, leading to a reduction in pressure loss during the delivery stage [54]. Yet, an overabundance of clay particles can inadvertently increase the viscosity of the mix, thereby negatively impacting the flow rate of the pump [55]. On the other hand, the presence of coarse granules in the mix is crucial to enhance the mixture's rigidity by increasing interparticle friction [56]. Therefore, designing an optimal mix for 3D printing of soils necessitates a well-considered balance of these components. The best mix should harmoniously integrate the benefits of both clay and coarse particles, achieving a balance that optimizes both flow and stability for successful 3D printing.

3.2.3. in-situ stability in the green state

While the stability of deposited layers is commonly associated with their rigidity, there is a need to introduce a more comprehensive design methodology to ensure layer stability in-situ. With this goal in mind, an analytical model, proposed by Kruger et al. for cement-based materials, was applied in this study [31]. The utilization of this model facilitates a more intricate understanding of layer stability, anchored on the analysis of the rheometer test, which can consequently improve the

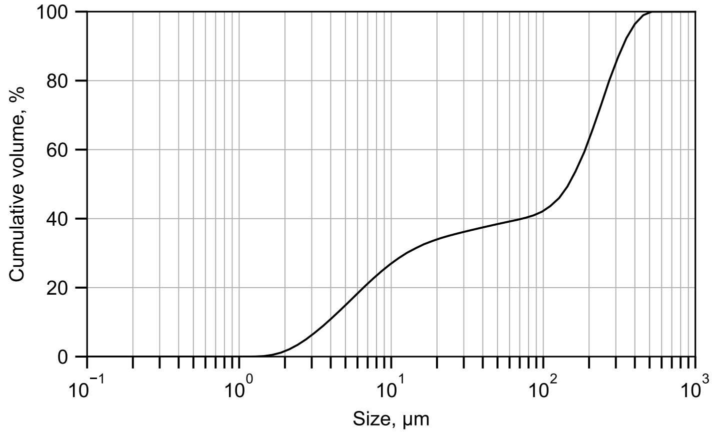

Figure 11: Grading curve representing the optimal composition of the white clay-sand mixture, yielding the best balance between flow and rigidity.

design strategy. The shear stress at the bottom layer, at which yielding occurred, can be calculated as follows [31]:

$$\tau = \frac{\rho g h}{2F_{AR}} \tag{4}$$

Where τ is the shear stress (Pa), g is the gravitational acceleration (m/s^2), h is the element height (m), and F_{AR} is a strength correction factor that accounts for confinement due to the layer aspect ratio (h/w).

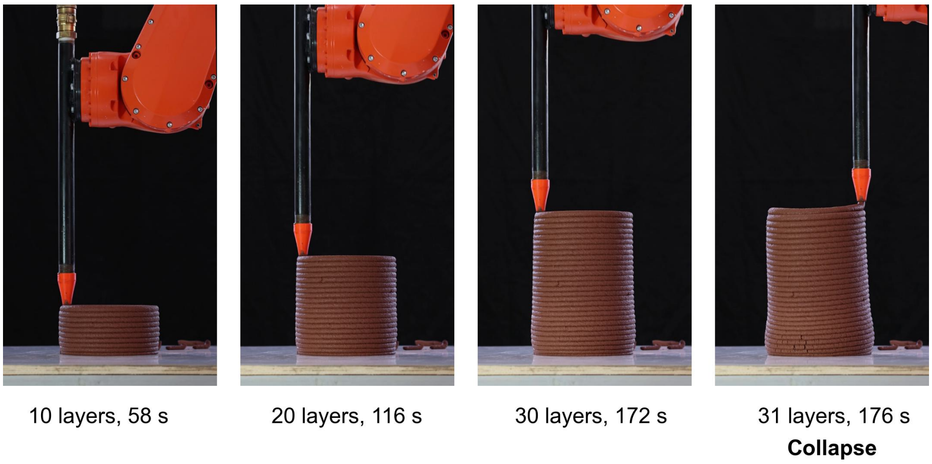

Figure 12: Chocolate clay mix cylindrical column printing until collapse for a 180 mm diameter. Left to right: 10 layers, 20 layers and 30 layers high cylinder and during collapse.

Controlled experiments were conducted, where a cylinder was printed until collapse to determine the point at which the bottom layer yields to the weight of the overlying layers (Figure 12). Three mixtures were examined at this stage, with White, Chocolate, and Mamshit clays. The three mixtures were prepared based on the optimal mixture outlined in Section 3.2. Each mix contained 2:5 clay/sand wt.% ratio. The clay/water ratio differed for each mix and was adjusted to achieve a spread of 140-145 mm in the flow table test after 25 jolts, as detailed in Table 3. A rheometer test (as described in Section 2) was conducted on each mixture after preparation, and the results are depicted in Figure 13. The printing test was repeated three times for each mix. The cylinder printing process parameters are described in Table 4.

Table 3: Composition of tested White, Chocolate, and Mamshit clay-sand mixtures.

Mix	**Clay (wt.%)**	**Sand (wt.%)**	**Water (wt.%)**
White	24.80159	62.00396825	13.19444444
Chocolate	25.15723	62.89308176	11.94968553
Mamshit	23.87205	59.68011459	16.44783958

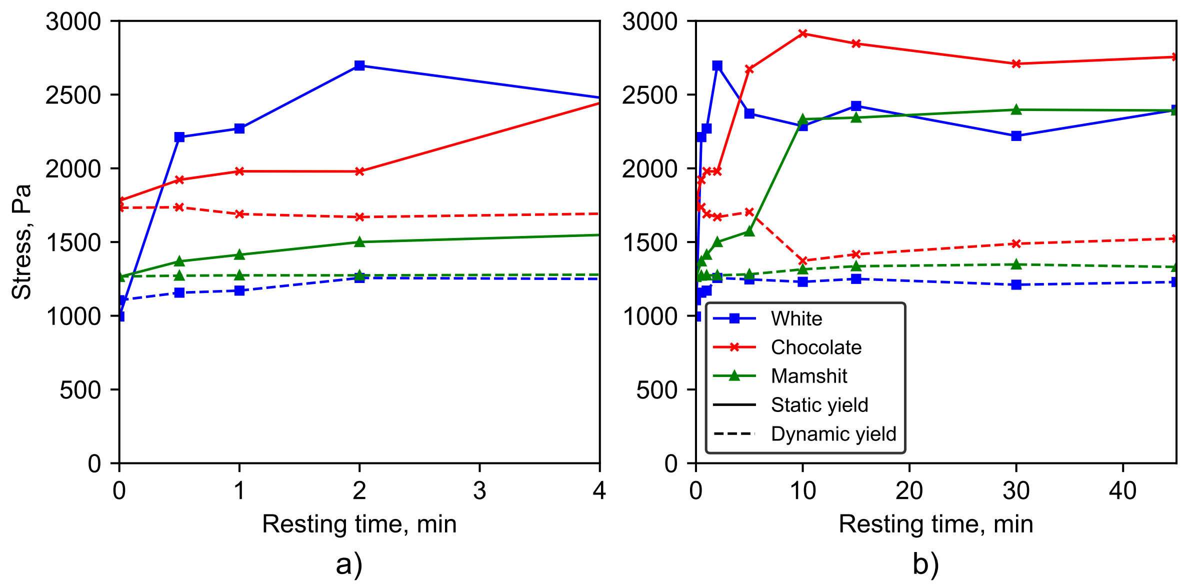

Figure 13: Influence of clay type on the rheological behavior of clay-sand mixtures (28.6% clay content). a) 0 to 4 minutes resting time, b) 0 to 45 minutes resting time.

Table 4: Cylinder printing process parameters

Diameter (mm)	**Nozzle velocity (mm/s)**	**Layer height (mm)**	**Layer width (mm)**	**Aspect ratio**	**Strength correction factor**	**Shear stress buildup (Pa/min)**
180	100	10	20	0.5	1.4	730

Consequently, based on equation 4 and under the specified conditions, the buildup rate of shear stress on the lower layer of the printed cylinder is 730 Pa/min. The intersection point of the plots obtained by plotting the shear stress buildup rate against the static yield of the tested material, as recorded by the rheometer test, can be used to predict cylinder collapse. For example, a cylinder printed with the Chocolate clay mix at the described conditions is calculated to collapse at 3.04 minutes, i.e., 184 seconds.

For the Chocolate clay mix an average failure time of 2.92 minutes was recorded, with a 6.8% coefficient of variation. The average number of layers at failure was found to be 32. The deviation between the predicted and measured values were 4.11% suggesting a good fit with the analytical model 14. This is agreeable with failure prediction of cement-based materials [31]. Across all experiments, it was observed that failure was consistently due to the plastic collapse of the lower layer [57]. Interestingly, an elastic buckling deformation was noted during the printing of the cylinder, which could potentially lead to distortions in the overall shape of the element (as illustrated in Figure 12).

To delve deeper into the failure mechanism and ascertain the critical strain values of the four lowermost layers, a digital image correlation analysis was performed as shown in Figure 15. This analysis results between 100 to 180 second window of the printing process are depicted in Figure 16. The data reveals a direct correlation between the increasing dead weight on a layer and its deformation, with the greatest deformations seen in the lowest layer. This supports the assertion that the cylinder's failure is triggered by the yield of the lower layer when a critical strain threshold is surpassed.

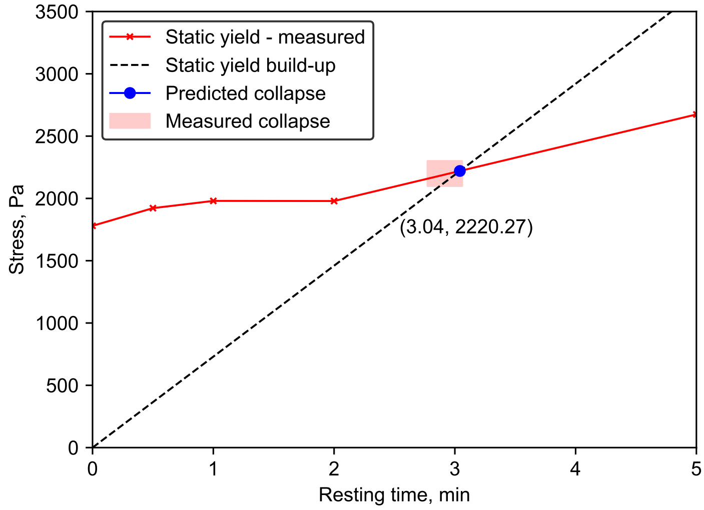

Figure 14: Intersection of calculated shear stress build-up at the bottom layer and characteristic shear yield strength for Chocolate clay mix, depicted for a 180 mm diameter cylindrical column.

371 Furthermore, the analysis discerns two distinct regimes during the printing process. The first regime exhibits elastic behavior, demonstrated by the relatively linear slope of the strain, persisting until the strain reaches a value of approximately 0.15 for the lowermost layer, or 140 seconds. The second regime is characterized by plastic deformation, evidenced by the exponential rise in strain leading up to the point of total collapse.

The outcomes of this test demonstrate that the presented approach provides a sound estimation of the mechanical dynamics occurring during the printing process. As such, it lays the foundation

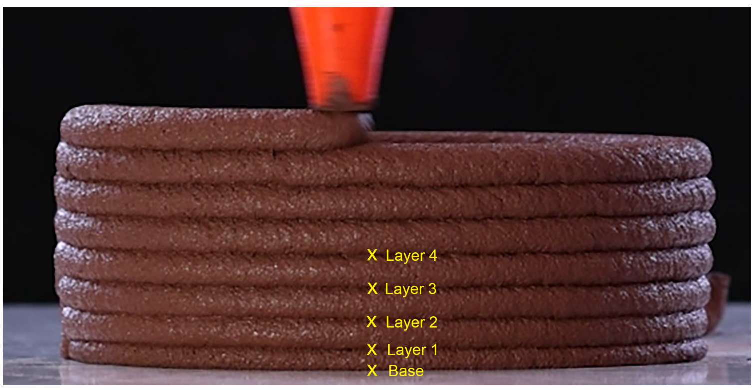

Figure 15: Digital Image Correlation (DIC) analysis illustrating based on layers strain during the 3D printing process.

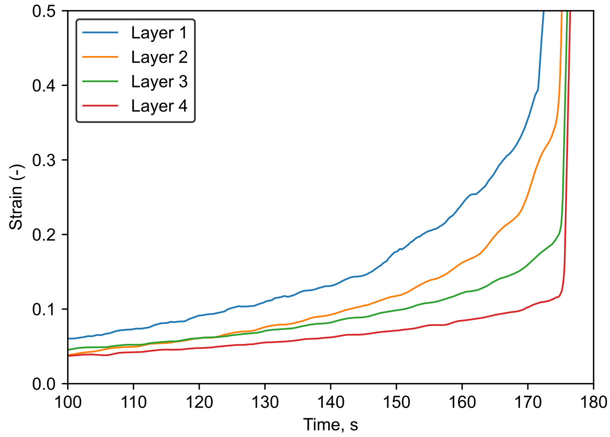

Figure 16: Lower layer strain during 180 mm cylinder printing until collapse for Chocolate clay mixture.

for developing a comprehensive design methodology for the entire printing operation. For example, considering a specific material and design, adjusting the nozzle speed could enhance the element's stability by granting more time for the consolidation of the mixture [6]. Alternatively, the mixture could be modified to better suit the element static yield build-up. This could be achieved by treating the soil with various stabilizers [29, 41, 35], thereby tailoring the mixture's properties to the demands of the process.

3.2.4. Effect of clay composition on stability in the green state

The three clays examined in this study vary in their mineralogical composition, particularly in terms of kaolinite content: 99.3%, 76.8%, and 41.5% for the White, Chocolate, and Mamshit clays, respectively, as detailed in Table 1.

The static yield achieved is similar for all three clay types as demonstrated in Figure 13, with Chocolate clay mix exhibiting slightly higher values. This may be attributed to its coarser and wider particle size distribution (Figure 17), which may facilitate a more efficient and denser packing. Additionally, the Chocolate clay mix has a greater proportion of silt-sized particles, which may increase the interparticle friction and consequently, the static yield of the mix.

There is, however, a considerable difference in the build-up of the static yield which is quickest in the White clay and slowest in the Mamshit clay (Figure 13a.), 2, 5 and 10 minutes for the White, Chocolate and Mamshit clay respectively. This could be correlated with the kaolinite content in each of them. The charged plate-shaped particles of kaolinite form a card-house structure increasing the thixotropic effect of the mix [58]. The individual kaolinite particles, with their layered structure and net negative charge, are capable of establishing strong, electrostatic interactions with surrounding particles and water molecules. This contributes to the formation of a stable, gel-like network in the mixture, thereby augmenting its thixotropic behavior [59]. Furthermore, the size and shape of kaolinite particles also play a vital role in promoting thixotropy. The thin, platy morphology of kaolinite particles leads to high specific surface area and facilitates the formation of a closely-knit, coherent microstructure in the mixture [60]. This structure enhances resistance against deformation, contributing to the rapid build-up of static yield stress.

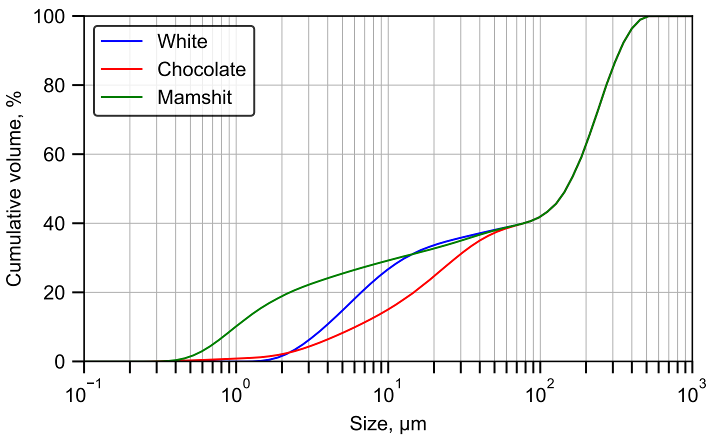

Figure 17: Particle size distribution of the tested clay-sand mixes.

To assess the influence of various clay compositions and gradings on the 3D printing performance of the artifact, in-situ stability tests were conducted on each mix using the cylindrical column printing method. The evolution of static yield and the intersection with shear stress buildup at the lowest layer are displayed in Figure 18. Images taken during the photographic monitoring of the printing process until column collapse are provided in Figure 19.

Differences in static yield evolution among the mixes became evident in the initial minutes of the test. The Mamshit clay mix, which contained the largest volume of clay sized particles, collapsed the quickest, on average, after 2.5 minutes (4.2% variation, 21% deviation from the analytical model). The chocolate clay mix collapsed within 2.92 minutes (5.1% variation, 4.11%

deviation), while the collapse of the white clay mix took place after 3.2 minutes (6.8% variation, 7.7% deviation).

The results demonstrate that the analytical model aligns with the trends observed in the rheological test, and effectively predicts the point of collapse for the cylinder across several tested soils. The pronounced deviation witnessed in the Mamshit clay mix from the analytical model could be attributed to sensitivities tied to the rheological test procedure. This divergence can be addressed by refining the procedure of the rheological test and by allowing the mix to homogenize over several days prior to conducting the various tests. This approach should ensure a more consistent mixture, potentially leading to more accurate predictions.

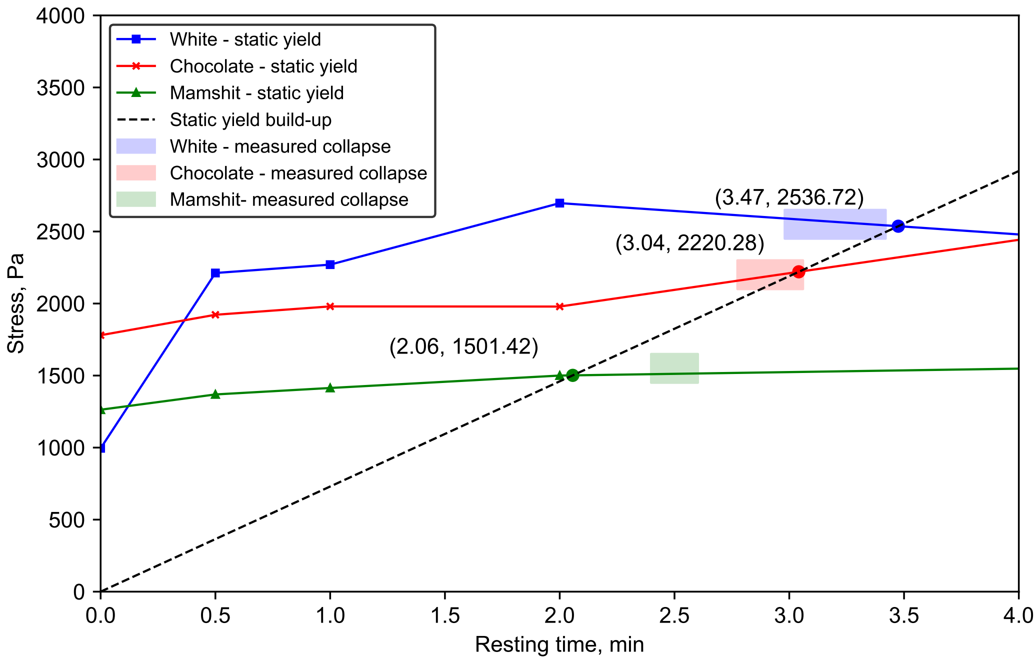

Figure 18: Comparison of calculated shear stress build-up and characteristic shear yield strength for three different clay mixes in a 180 mm diameter cylindrical column. The values calculated based on the intersection point of the two curves are shown. The highlighted boxes indicate the range of measured values for collapse time.

3.2.5. Effect of clay composition on mechanical properties

Figure 20 shows the mechanical characterization results for the various soils tested. In contrast to stability in the green state, the highest compressive strength values were observed in the Mamshit

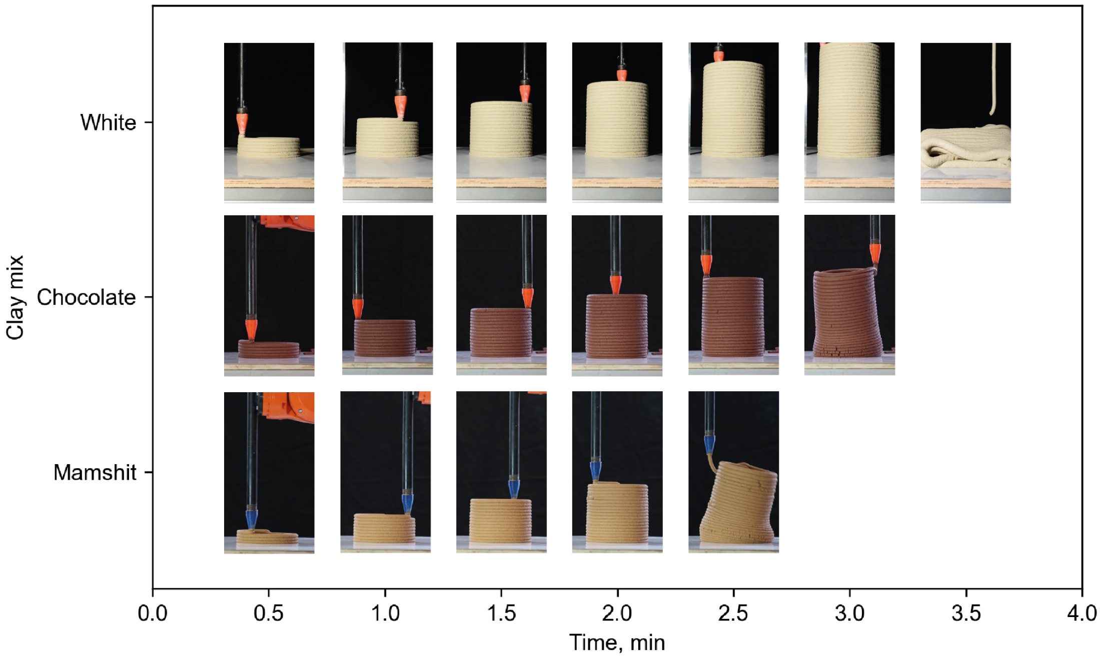

Figure 19: In-situ stability test via cylindrical column printing of the three tested clay-sand mixes. The printing process is described in 30-second intervals until collapse.

clay mix, followed by the Chocolate clay mix, with the White mix demonstrating the lowest values. Similarities were found in the flexural test results for both Mamshit and Chocolate clay mixes, but these were notably lower for the White mix.

The outcomes of the compressive strength tests suggest an absence of direct correlation between the kaolinite content and the strength of the mixture, unlike its relation with the static yield buildup rate. However, the particle grading appears to hold a significant influence over the strength of the mixture, which is consistent with the results described by Cuccurullo et al. [61]. The Mamshit clay mixture, which contains a larger fraction of clay-sized particles, rather than clay-mineral particles, is likely to have prompted a denser microstructural arrangement of its constituent granules, thereby resulting in a more structurally robust mixture. The Chocolate clay mixture, characterized by a coarser particle grading, could potentially enhance the frictional resistance between particles, thus yielding positive outcomes.

The results from the mechanical characterization imply a potential contradiction between the green and hardened state properties when optimizing clay-based mixtures for 3D printing applications. While some mixtures may exhibit enhanced properties in the green state, such as an increased rate of static yield buildup, these may not necessarily correspond with an augmentation of improved mechanical properties. Notwithstanding, strategies for soil stabilization, might provoke a synergistic effect capable of improving both the green and hardened state properties.

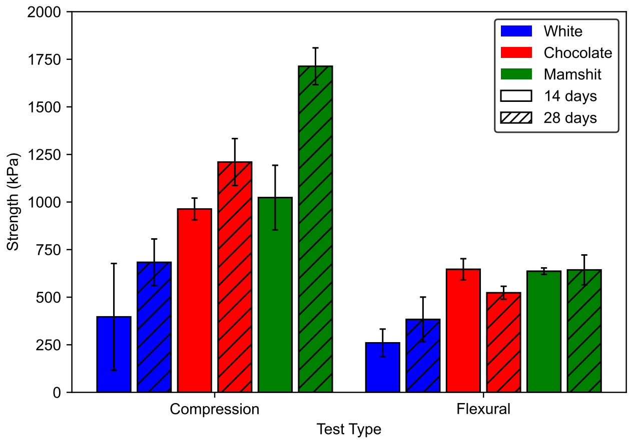

Figure 20: Compressive and flexural strengths of the tested mixes at 14- and 28-days.

4. Conclusions

The presented study offers valuable guidelines for designing mixtures for 3D printing of clay-based soils in construction and architecture.

Performance and rheological tests were conducted on various ratios of clay/sand and clay/water. The results of these tests revealed significant linear correlations, highlighting essential performance metrics for evaluating the mix. The analysis identified a robust linear relationship between a custom rigidity test and static yield stress, as well as between the flow table test and flow rate through the pump. These findings suggest that a simple flow table test, combined with a custom-built rigidity test, offers a sufficient and cost-effective method for the evaluation of soil-based material properties for 3D printing.

Basic rheological parameters were verified using an analytical model to predict the green state's stability during 3D printing. This was achieved by 3D printing a cylinder model at constant velocity until collapse. Plastic collapse was observed for all mixtures due to bottom layer yield. The in-situ stability test provides a practical framework for fine-tuning printing parameters and layer geometry to avoid plastic collapse. The results of this test suggest the printing parameters should be adapted according to the material rheological properties and printed artifact scale. Additionally, the in-situ test was completed by a digital image correlation analysis, revealing critical strain in the bottom layer as the driving force for the printed cylinder plastic collapse.

Finally, the results of the study highlight the influence of particle size distribution and clay mineralogy on material performance in 3D printing. It was observed that an increased presence of the kaolinite mineral could trigger a more pronounced thixotropic effect at the re-flocculation stage, facilitating quicker static yield evolution and therefore delaying the structure collapse. Furthermore, a coarser particle size distribution enhanced static yield value of the tested mix.

Future work in this area should focus on better understanding and improving the thixotropy of the mixtures, in order to optimize the design of soil-based materials for 3D printing. Such studies could refine the material's short-term thixotropy using stabilizing agents, which would otherwise be limited, enabling faster construction rates. These modifications, however, should maintain low dynamic rheological values, specifically the dynamic yield value and viscosity, to ensure a smooth pumping stage. Furthermore, a micro-structural investigation into the effects of soil mineralogy and particle grading on both short and long-term rheological properties of the mixture could provide insights into the design strategies of soil-based materials for 3D printing. Additionally, it is imperative that methods for optimizing these short-term rheological properties go hand in hand with enhancing the material's long-term attributes, such as compressive and flexural strength, as well as durability. As these efforts progress, it is crucial to consider the environmental impact of any mineral or bio-based additives, ensuring that the soil remains a low-impact and recyclable material

5. Data Availability Statement

Some or all data that support the findings of this study are available from the corresponding author upon reasonable request.

6. Acknowledgments

The authors gratefully acknowledge the generous funding provided by the Israel Ministry of Housing and Construction under grant no. 2031203. This financial support has been instrumental in enabling this research.

Additionally, this research benefited immensely from the support of the National Building Research Institute (Israel) staff. Their dedication and cooperation are greatly acknowledged. Finally, We would like to extend our sincere gratitude to Research Assistant Tair Shekel for her assistance in preparing some of the illustrations presented in this paper.

References

[1] K. L. Bar-Sinai, T. Shaked, A. Sprecher, Robotic tools, native matter: workflow and methods for geomaterial reconstitution using additive manufacturing, Architectural Science Review 64 (6) (2021) 490–503.

[2] A. Veliz Reyes, W. Jabi, M. Gomaa, A. Chatzivasileiadi, L. Ahmad, N. M. Wardhana, Negotiated matter: a robotic exploration of craft-driven innovation, Architectural Science Review 62 (5) (2019) 398–408.

[3] J.-B. Izard, A. Dubor, P.-E. Hervé, E. Cabay, D. Culla, M. Rodriguez, M. Barrado, Large-scale 3d printing with cable-driven parallel robots, Construction Robotics 1 (2017) 69–76.

[4] M. Gomaa, W. Jabi, A. V. Reyes, V. Soebarto, 3d printing system for earth-based construction: Case study of cob, Automation in Construction 124 (2021) 103577. doi:10.1016/J.AUTCON.2021.103577.

[5] G. Vantyghem, W. De Corte, E. Shakour, O. Amir, 3d printing of a post-tensioned concrete girder designed by topology optimization, Automation in Construction 112 (2020) 103084.

[6] M. Mogra, O. Asaf, A. Sprecher, O. Amir, Design optimization of 3d printed concrete elements considering buildability, Engineering Structures 294 (2023) 116735.

[7] I. Agustí-Juan, G. Habert, Environmental design guidelines for digital fabrication, Journal of cleaner production 142 (2017) 2780–2791.

[8] J.-C. Morel, A. Mesbah, M. Oggero, P. Walker, Building houses with local materials: means to drastically reduce the environmental impact of construction, Building and environment 36 (10) (2001) 1119–1126.

[9] A. Shukla, G. Tiwari, M. Sodha, Embodied energy analysis of adobe house, Renewable Energy 34 (3) (2009) 755–761.

[10] J.-C. Morel, R. Charef, E. Hamard, A. Fabbri, C. Beckett, Q.-B. Bui, Earth as construction material in the circular economy context: practitioner perspectives on barriers to overcome, Philosophical Transactions of the Royal Society B 376 (1834) (2021) 20200182.

[11] D. Ardant, C. Brumaud, A. Perrot, G. Habert, Robust clay binder for earth-based concrete, Cement and Concrete Research 172 (2023) 107207.

[12] O. Kontovourkis, G. Tryfonos, Robotic 3d clay printing of prefabricated non-conventional wall components based on a parametric-integrated design, Automation in Construction 110 (2020) 103005.

[13] S. Barnes, L. Kirssin, E. Needham, E. Baharlou, D. E. Carr, J. Ma, 3d printing of ecologically active soil structures, Additive Manufacturing 52 (2022) 102670. doi:10.1016/J.ADDMA.2022.102670.

[14] H. Alhumayani, M. Gomaa, V. Soebarto, W. Jabi, Environmental assessment of large-scale 3d printing in construction: A comparative study between cob and concrete, Journal of Cleaner Production 270 (2020) 122463. doi:10.1016/J.JCLEPRO.2020.122463.

[15] A. Chiusoli, 3D printed house TECLA - Eco-housing — 3D Printers — WASP — 3dwasp.com, `https://www.3dwasp.com/en/3d-printed-house-tecla/`, [Accessed 17-08-2023] (2021).

[16] A. Ellery, Sustainable in-situ resource utilization on the moon, Planetary and Space Science 184 (5 2020). doi:10.1016/j.pss.2020.104870.

[17] S. Pilehvar, M. Arnhof, R. Pamies, L. Valentini, A. L. Kjøniksen, Utilization of urea as an accessible superplasticizer on the moon for lunar geopolymer mixtures, Journal of Cleaner Production 247 (2 2020). doi:10.1016/j.jclepro.2019.119177.

[18] S. Qaidi, A. Yahia, B. Tayeh, H. Unis, R. Faraj, A. Mohammed, 3d printed geopolymer composites: A review, Materials Today Sustainability 20 (2022) 100240. doi:https://doi.org/10.1016/j.mtsust.2022.100240. URL `https://www.sciencedirect.com/science/article/pii/S2589234722001324`

[19] M. Gomaa, W. Jabi, V. Soebarto, Y. M. Xie, Digital manufacturing for earth construction: A critical review, Journal of Cleaner Production 338 (2022) 130630. doi:10.1016/J.JCLEPRO.2022.130630.

[20] N. Labonnote, A. Rønnquist, B. Manum, P. Rüther, Additive construction: State-of-the-art, challenges and opportunities, Automation in construction 72 (2016) 347–366.

[21] M. T. Souza, I. M. Ferreira, E. G. de Moraes, L. Senff, A. P. N. de Oliveira, 3d printed concrete for large-scale buildings: An overview of rheology, printing parameters, chemical admixtures, reinforcements, and economic and environmental prospects, Journal of Building Engineering 32 (2020) 101833.

[22] V. Mechtcherine, F. P. Bos, A. Perrot, W. R. da Silva, V. N. Nerella, S. Fataei, R. J. Wolfs, M. Sonebi, N. Roussel, Extrusion-based additive manufacturing with cement-based materials – production steps, processes, and their underlying physics: A review, Cement and Concrete Research 132 (2020) 106037. doi:10.1016/J.CEMCONRES.2020.106037.

[23] K. Kovler, N. Roussel, Properties of fresh and hardened concrete, Cement and Concrete Research 41 (7) (2011) 775–792.

[24] Y. Qian, S. Kawashima, Distinguishing dynamic and static yield stress of fresh cement mortars through thixotropy, Cement and Concrete Composites 86 (2018) 288–296.

[25] G. D. Schutter, D. Feys, Pumping of fresh concrete: Insights and challenges, RILEM Technical Letters 1 (2016) 76–80. doi:10.21809/rilemtechlett.2016.15.

[26] E. Buckingham, On plastic flow through capillary tubes, in: Proc. Am. Soc. Testing Materials, 1921, pp. 1154–1156.

[27] F. Bos, R. Wolfs, Z. Ahmed, T. Salet, Additive manufacturing of concrete in construction: potentials and challenges of 3d concrete printing, Virtual and Physical Prototyping 11 (2016) 209–225. doi:10.1080/17452759.2016.1209867.

[28] R. A. Buswell, W. R. L. de Silva, S. Z. Jones, J. Dirrenberger, 3d printing using concrete extrusion: A roadmap for research, Cement and Concrete Research 112 (2018) 37–49. doi:10.1016/J.CEMCONRES.2018.05.006.

[29] A. Perrot, D. Rangeard, E. Courteille, 3d printing of earth-based materials: Processing aspects, Construction and Building Materials 172 (2018) 670–676. doi:10.1016/j.conbuildmat.2018.04.017.

[30] N. Roussel, Rheological requirements for printable concretes, Cement and Concrete Research 112 (2018) 76–85. doi:10.1016/J.CEMCONRES.2018.04.005.

[31] J. Kruger, S. Zeranka, G. van Zijl, 3d concrete printing: A lower bound analytical model for buildability performance quantification, Automation in Construction 106 (10 2019). doi:10.1016/j.autcon.2019.102904.

[32] J. Kruger, M. Van den Heever, S. Cho, S. Zeranka, G. Van Zijl, High-performance 3d printable concrete enhanced with nanomaterials, in: Proceedings of the international conference on sustainable materials, systems and structures (SMSS 2019), Vol. 533, 2019, pp. 533–540.

[33] J. Kruger, S. Cho, S. Zeranka, C. Viljoen, G. van Zijl, 3d concrete printer parameter optimisation for high rate digital construction avoiding plastic collapse, Composites Part B: Engineering 183 (2020) 107660.

[34] A. Biggerstaff, M. Lepech, G. Fuller, D. Loftus, A shape stability model for 3d printable biopolymer-bound soil composite, Construction and Building Materials 321 (2022) 126337. doi:10.1016/J.CONBUILDMAT.2022.126337.

[35] A. Biggerstaff, G. Fuller, M. Lepech, D. Loftus, Determining the yield stress of a biopolymer-bound soil composite for extrusion-based 3d printing applications, Construction and Building Materials 305 (2021) 124730. doi:10.1016/J.CONBUILDMAT.2021.124730.

[36] A. Bajpayee, M. Farahbakhsh, U. Zakira, A. Pandey, L. A. Ennab, Z. Rybkowski, M. K. Dixit, P. A. Schwab, N. Kalantar, B. Birgisson, S. Banerjee, In situ resource utilization and reconfiguration of soils into construction materials for the additive manufacturing of buildings, Frontiers in Materials 7 (3 2020). doi:10.3389/fmats.2020.00052.

[37] G. Silva, R. Ñañez, D. Zavaleta, V. Burgos, S. Kim, G. Ruiz, M. A. Pando, R. Aguilar, J. Nakamatsu, Eco-friendly additive construction: Analysis of the printability of earthen-based matrices stabilized with potato starch gel and sisal fibers, Construction and Building Materials 347 (2022) 128556.

[38] G. Bai, L. Wang, G. Ma, J. Sanjayan, M. Bai, 3d printing eco-friendly concrete containing under-utilised and

waste solids as aggregates, Cement and Concrete Composites 120 (2021) 104037.

[39] A. Alqenaee, A. Memari, Experimental study of 3d printable cob mixtures, Construction and Building Materials 324 (2022) 126574.

[40] E. Ferretti, M. Moretti, A. Chiusoli, L. Naldoni, F. De Fabritiis, M. Visonà, Rice-husk shredding as a means of increasing the long-term mechanical properties of earthen mixtures for 3d printing, Materials 15 (3) (2022) 743.

[41] F. Faleschini, D. Trento, M. Masoomi, C. Pellegrino, M. A. Zanini, Sustainable mixes for 3d printing of earth-based constructions, Construction and Building Materials 398 (2023) 132496.

[42] P. Narloch, P. Woyciechowski, J. Kotowski, I. Gawriuczenkow, E. Wójcik, The effect of soil mineral composition on the compressive strength of cement stabilized rammed earth, materials 13 (2020). doi:10.3390/ma13020324. URL www.mdpi.com/journal/materials

[43] G. Minke, Building with Earth: Design and Technology of a Sustainable Architecture, 3rd Edition, Birkhäuser, 2012. doi:doi:10.1515/9783034608725. URL https://doi.org/10.1515/9783034608725

[44] A. Ammari, K. Bouassria, M. Cherraj, H. Bouabid, S. Charif D'ouazzane, Combined effect of mineralogy and granular texture on the technico-economic optimum of the adobe and compressed earth blocks, Case Studies in Construction Materials 7 (2017) 240–248. doi:https://doi.org/10.1016/j.cscm.2017.08.004. URL https://www.sciencedirect.com/science/article/pii/S2214509517300827

[45] ASTM International, ASTM C230/C230M - 20: Standard Specification for Flow Table for Use in Tests of Hydraulic Cement, Standard C230/C230M - 20, ASTM International, accessed: 2023-05-08 (2020). URL https://www.astm.org/Standards/C230.htm

[46] A. Kazemian, X. Yuan, E. Cochran, B. Khoshnevis, Cementitious materials for construction-scale 3d printing: Laboratory testing of fresh printing mixture, Construction and Building Materials 145 (2017) 639–647. doi:10.1016/J.CONBUILDMAT.2017.04.015.

[47] J. Lee Rodgers, W. A. Nicewander, Thirteen ways to look at the correlation coefficient, The American Statistician 42 (1) (1988) 59–66.

[48] Y. Ren, S. Yang, K. H. Andersen, Q. Yang, Y. Wang, Thixotropy of soft clay: A review, Engineering Geology 287 (6 2021). doi:10.1016/j.enggeo.2021.106097.

[49] X. W. Zhang, L. W. Kong, A. W. Yang, H. M. Sayem, Thixotropic mechanism of clay: A microstructural investigation, Soils and Foundations 57 (2017) 23–35. doi:10.1016/j.sandf.2017.01.002.

[50] A. Perrot, D. Rangeard, A. Pierre, Structural built-up of cement-based materials used for 3d-printing extrusion techniques, Materials and Structures (2016) 1213–1220doi:10.1617/s11527-015-0571-0.

[51] R. Wolfs, F. Bos, T. Salet, Early age mechanical behaviour of 3d printed concrete: Numerical modelling and experimental testing, Cement and Concrete Research 106 (2018) 103–116.

[52] S. Cytryn, SOIL CONSTRUCTION, its principles and application for Housing, Vol. 5, The Weizman Science

Press of Israel, 1958.

[53] M. C. J. Delgado, I. C. Guerrero, The selection of soils for unstabilised earth building: A normative review, Construction and Building Materials 21 (2007) 237–251. doi:10.1016/J.CONBUILDMAT.2005.08.006.

[54] S. D. Jo, C. K. Park, J. H. Jeong, S. H. Lee, S. H. Kwon, A computational approach to estimating a lubricating layer in concrete pumping, CMC 27 (2012) 189–210.

[55] M. Westerholm, B. Lagerblad, J. Silfwerbrand, E. Forssberg, Influence of fine aggregate characteristics on the rheological properties of mortars, Cement and Concrete Composites 30 (4) (2008) 274–282.

[56] J. Gong, X. Wang, L. Li, Z. Nie, Dem study of the effect of fines content on the small-strain stiffness of gap-graded soils, Computers and Geotechnics 112 (2019) 35–40.

[57] A. S. Suiker, R. J. Wolfs, S. M. Lucas, T. A. Salet, Elastic buckling and plastic collapse during 3d concrete printing, Cement and Concrete Research 135 (2020) 106016.

[58] V. Gupta, M. A. Hampton, J. R. Stokes, A. V. Nguyen, J. D. Miller, Particle interactions in kaolinite suspensions and corresponding aggregate structures, Journal of Colloid and Interface Science 359 (1) (2011) 95–103. doi:https://doi.org/10.1016/j.jcis.2011.03.043.
URL https://www.sciencedirect.com/science/article/pii/S0021979711003195

[59] R. Ran, S. Pradeep, S. K. Acharige, B. C. Blackwell, C. Kammer, D. J. Jerolmack, P. E. Arratia, Understanding the rheology of kaolinite clay suspensions using bayesian inference, Journal of Rheology 67 (2023) 241–252. doi:10.1122/8.0000556.

[60] E.-J. Teh, Y.-K. Leong, Y. Liu, A. Fourie, M. Fahey, Differences in the rheology and surface chemistry of kaolin clay slurries: The source of the variations, Chemical Engineering Science 64 (17) (2009) 3817–3825.

[61] A. Cuccurullo, D. Gallipoli, A. W. Bruno, C. Augarde, P. Hughes, C. L. Borderie, A comparative study of the effects of particle grading and compaction effort on the strength and stiffness of earth building materials at different humidity levels, Construction and Building Materials 306 (2021) 124770. doi:10.1016/J.CONBUILDMAT.2021.124770.